

# **InGaAs/InP quantum well intermixing studied by cross-sectional scanning tunneling microscopy**

Huajie Chen and R. M. Feenstra

Department of Physics, Carnegie Mellon University, Pittsburgh, Pennsylvania  
15213

G. C. Aers, P. J. Poole, R. L. Williams and S. Charbonneau  
Institute for Microstructural Sciences, National Research Council of Canada,  
Ottawa, K1A0R6, Canada

P. G. Piva, R. D. Goldberg and I. V. Mitchell  
Department of Physics and Astronomy, University of Western Ontario, London  
N6A3K7, Canada

## **Abstract**

Cross-sectional scanning tunneling microscopy (STM) is used to study lattice matched InGaAs/InP quantum well (QW) intermixing induced by ion implantation and thermal annealing. Different strain development in QWs (determined by STM topography of elastic relaxation in cross-sectionally cleaved samples) is found to be dependent upon the range of the implanted ions relative to the QWs. It is found that the quantum wells remain latticed matched to the barrier layers after intermixing when ions are implanted through the multiple quantum well (MQW) stack. A shallow implantation in which ions are implanted into the cap layer above the MQW stack leads to tensilely strained wells and compressively strained interfaces between wells and barriers. The strain development in the latter case is attributed to different degrees of interdiffusion on the group III and group V sublattices. Finite element elastic computations are used to extract the group V and group III interdiffusion length ratio, and results using different diffusion models are compared. A preferred group V interdiffusion in the case of shallow implantation is explained in terms of faster diffusing P related defects compared to In related defects. Images of as-grown QWs provide useful information about the growth-technique related compositional fluctuations at the interfaces.

## **1 INTRODUCTION**

Interdiffusion of quantum well (QW) structures [1] has recently been investigated as a means of integrating regions of different band gaps in the same epitaxial layer for photonic integrated device applications [2]. However, greater knowledge of the microscopic mechanisms of QW intermixing is required to optimize this process. Techniques traditionally used to study QW intermixing include transmission electron microscopy (TEM), photoluminescence (PL) and x-ray diffraction (XRD). In this paper, we show how cross-sectional scanning tunneling microscopy (STM) can be used to study this subject.

Cross-sectional STM of III-V semiconductors has been proven to be a very powerful tech-

nique [3]. It is based on the fact that it is relatively easy to obtain a flat (110) cleavage face, and the cleaved surface is not reconstructed. This allows bulk (*i.e.* non-surface-specific) information to be obtained on an atomic scale by studying the cleaved surface. Typical applications include observation of point defects, heterostructure interfaces, and band offsets [3].

Figure 1 shows a typical cross-sectional STM image. The image was taken from an InGaAs/InP multiple quantum well (MQW) structure. All the images and surface profiles in this paper are presented with the growth direction from right to left. The wider layers seen in Fig. 1 are InP barriers, and the narrower layers are InGaAs wells. The latter appear as mottled white and black because of fluctuations in the alloy composition. There are a few white spots across the image which are Si dopant atoms. The atomic corrugation of the InP layers is seen as fine periodic lines parallel to the QWs with a spacing of 0.587 nm (every second bilayer is imaged on the (110) surface).

Recently it was demonstrated by the current authors that cross-sectional scanning probe microscopy can also be used to reveal strain information in the bulk [4-6]. Because of strain, the cleaved surface will elastically relax. For the case of a periodically varying strain (in the (001) direction here) this relaxation will produce an undulation of the surface, which is directly measurable by STM or atomic force microscopy (AFM). Combined with finite element elastic computation, quantitative information about the strain can be obtained.

In this paper, a detailed comparative study of samples primarily from two different wafers is presented. The samples were implanted with P ions to produce a large concentration of defects, which diffuse through the sample causing QW intermixing during subsequent annealing. Wafer A has a thin InP cap layer and P ions are implanted *through* the MQW stack. No evidence of strain development is observed in this case, suggesting that group V (anion) and group III (cation) atoms intermix at similar rates. For wafer B, P ions are implanted into a thick cap layer above the MQW stack, without reaching the MQW stack. Contrary to the results from sample A, significant strain development is observed across the QW structure. Figure 2 illustrates the structures and implantation ranges of the two types of samples. Finite element calculations, coupled with a QW interdiffusion model, are carried out to model the strain profile produced by different group V and group III interdiffusion rates. It is also found that the data is more consistent with a simple square well interdiffusion model than with conventional Fickian interdiffusion. We propose that the variation in strain development with different implantation conditions is due to defects associated with the group V sublattice diffusing faster than group III sublattice defects. Finally, we show that STM can provide useful information about growth technique induced compositional fluctuations at the interfaces of as-grown QWs.

## 2 EXPERIMENT

The wafers used in this study were grown by Chemical Beam Epitaxy (CBE) in a RIBER CBE 32P reactor at a temperature of 490° C. The group III sources, TEGa and TMI, were introduced into the chamber using H<sub>2</sub> as the carrier gas. Pure AsH<sub>3</sub> and PH<sub>3</sub> were used as the group V sources, and were cracked at 950° C in a high temperature cell to produce predominantly As<sub>2</sub> and P<sub>2</sub>. The wafers were grown on an exact (100) oriented InP n-type (S-doped) substrate, and the grown layer was doped n-type with silicon using a conventional Knudsen-cell. Doping for wafer A and B is  $8 \times 10^{18} \text{ cm}^{-3}$  and  $2 \times 10^{17} \text{ cm}^{-3}$ , respectively. Doping is required to allow STM measurements to be made.

Both structures consist of a 20 period stack of nominally lattice-matched  $\text{In}_{0.53}\text{Ga}_{0.47}\text{As}$  QWs with InP barriers and capped with InP.

Ion implantation was carried out using a 1.7 MV Tandem accelerator. Portions of wafers A and B were implanted with 1 MeV and 500 keV phosphorus ions, respectively, at a substrate temperature of  $200^\circ\text{C}$  and  $7^\circ$  off-normal to minimize ion channeling. Ion flux and fluence were  $26\text{ nA cm}^{-2}$  and  $1\times 10^{14}\text{ ions cm}^{-2}$  respectively. Subsequent anneals, performed simultaneously on both as-grown and implanted samples, were done using a Heatpulse 610 rapid thermal annealer. A ramp rate of  $20^\circ\text{C s}^{-1}$  was used to reach the anneal temperatures. For wafer A, an anneal at  $675^\circ\text{C}$  for 90 s was selected to saturate the interdiffusion in the implanted sample whilst preserving the as-grown QW band gap of the unimplanted sample. Wafer B was initially given an anneal at  $675^\circ\text{C}$  for a period of 90 seconds, which resulted in a PL shift of less than 20 meV. A further anneal at  $725^\circ\text{C}$  for 90 seconds was thus required to ensure significant interdiffusion in the implanted samples, as indicated by PL, while essentially preserving the as-grown QW bandgap of the unimplanted material. STM images of samples from wafer B which received only a single anneal at  $740^\circ\text{C}$  for 90s are similar to those shown here after two anneals. During annealing, the sample surfaces were protected from In and P desorption by an InP proximity cap.

Low temperature (4.2K) continuous-wave PL measurements were performed to monitor changes in the QW band gap induced by the interdiffusion process. Samples were excited below the bulk InP band gap using an  $\text{Ar}^+$  pumped Ti:sapphire laser. Representative spectra are shown in Fig. 3 for the as-grown sample together with those obtained after rapid thermal annealing (RTA) only and after P ion-implantation followed by RTA. These spectra indicate that some slight intermixing occurred due to the RTA alone but that a very significant shift was induced by the implant generated point defects.

Cross-sectional STM measurements were performed in an ultra-high-vacuum chamber with base pressure  $< 5 \times 10^{-11}$  Torr. Tungsten probe tips, electrochemically etched and cleaned by electron bombardment, were used. The samples were cleaved *in situ* to expose a  $(\bar{1}10)$  crystal face. A constant tunnel current of 0.1 nA was used for STM imaging. Several cleaved samples were studied for each of the as-grown and implant+RTA samples, with separate probe tips used for each sample.

### 3 RESULTS

#### 3.1 STM Results

Figure 4 shows STM images of wafer A, each displaying one quantum well of the 20 period MQW stack (no significant differences are observed between layers throughout the stack). The InGaAs layers appear as the mottled black and white region in the center of each image. Their appearance arises from fluctuations in alloy composition of the ternary material. Results for the as-grown and implanted samples are shown in Figs. 4(a) and (b) respectively; both samples underwent the same RTA cycle. The image of the as-grown+RTA sample is very similar to that of an as-grown sample which was not annealed. As can be clearly seen from Fig. 4, intermixing occurs after implantation and annealing, and the QW becomes wider. The QW width is determined using a method described in Ref. [7], using the contrast between the different group III or V atoms in the alloy layer. The QW width of the as-grown+RTA sample is approximately 8.5 nm and that of the implant+RTA sample is 10.1 nm. Figures 4(c) and (d) show the vertical average of the images (a) and (b), respectively.

No significant change in local strain occurs during intermixing apart from a general smoothing of the surface profile.

Figure 5 shows a high resolution image of the as-grown+RTA sample. This image was taken with negative sample bias voltage, while the images in Fig. 4 were taken with positive bias voltage. The QW appears white in Fig. 5 due to an electronic effect in the STM imaging. As a result, it is easier to see the interfaces between well and barrier in this image. Note that the topographic minimum near the right-hand interface (InGaAs on InP) is slightly lower than that near the left-hand interface, by about  $0.13 \text{ \AA}$ . A similar asymmetry is seen in other STM images, at both positive and negative sample bias and for both as-grown and implanted samples; we return to this point in sections III C and D below. The remainder of the images presented in this paper were acquired with positive sample bias voltages, since in that case electronic effects in the STM images are small [6] and the tip height can be interpreted directly in terms of topographic variation (*i.e.* strain induced) of the sample surface.

STM images for sample B are shown in Fig. 6, each image displaying one quantum well of the 20 period MQW stack. Figure 6(a) shows the top layer (*i.e.* last grown layer) of the as-grown sample; Fig. 6(c) shows the bottom layer (first grown layer) of the as-grown sample; Figs. 6(b) and (d) show the top and bottom layers respectively of the implant+RTA sample. The width of the quantum wells of the as-grown sample is quite uniform throughout the 20 period stack, as can be seen in Figs. 6(a) and (c). Implantation induced intermixing between the InGaAs and InP layers is clearly seen in Figs. 6(b) and (d). A quantitative measurement of the alloy layer width is performed, with the resulting edges being indicated by the arrows. For the unimplanted sample, we find an alloy width of 6.0 nm, while in the implanted sample the width is found to be 8.2 nm for the top layer and 7.9 nm for the bottom layer. The similar extent of intermixing of the top and bottom layers (within a monolayer) indicates that the interdiffusion enhancing point defects can diffuse through  $0.48 \mu\text{m}$  of MQW material without significant trapping, and that the 40 InGaAs/InP interfaces have no obvious effect on the defect transport.

As clearly seen in Figs. 6(b) and (d), a white band appears near both well/barrier interfaces after intermixing. Figures 6(e) and (f) show the vertical average of images 6(c) and (d) respectively. The morphological undulation across the QW after intermixing is obvious. The white (higher tip height) contrast is seen for both positive and negative STM sample voltages, confirming that this feature is the primarily topographical in origin (as opposed to an electronic effect in the STM imaging). We assign this feature to the presence of a strained  $\text{InAs}_y\text{P}_{1-y}$  layer formed by preferred group V interdiffusion, with As and P interdiffusing while Ga and In show very little interdiffusion. Although the depth of the strain induced undulation, marked “A” in Fig. 6(f), may have both electronic and mechanical origins, the electronic effect at positive sample bias voltages used here is generally  $\lesssim 0.1 \text{ \AA}$  [6], so that the mechanical effect (*i.e.* elastic relaxation) dominates. A quantitative analysis of strain relaxation and a comparison of two different diffusion models are described in the next two sections.

### 3.2 Finite Element and Diffusion Calculations

The as-grown samples consist of  $\text{In}_{0.53}\text{Ga}_{0.47}\text{As}$  QWs which, according to x-ray measurements, are accurately lattice matched to the InP barrier layers (some interesting local deviations from lattice matching will be discussed in section III D). In general both group V and group III elements can

interdiffuse. If the group V and group III atoms interdiffuse at similar rates, the structure will remain locally lattice matched. However, strain will develop across the structure if the group V and group III elements diffuse at different rates. Various models have been proposed to describe the diffusion profile; for a given model one can calculate the energy band diagram, electron and hole confinement energies, and excitonic PL transition energies.

In this section we will explore two intermixing models, the commonly used Fickian model [8,9] and a square well model [10]. In the Fickian model, the diffusion follows Fick’s law, and the resulting concentration profile can be described by a double error function, with group V and group III elements having separate interdiffusion lengths  $\Delta_V$  and  $\Delta_{III}$ . We will define a diffusion length ratio  $\kappa \equiv \Delta_V/\Delta_{III}$ . Alternatively, as an illustration of extreme non-Fickian diffusion, the square well model assumes that the group V and group III element concentration is uniform in the QW (a picture in which interdiffusion is much faster in the QW than in the barrier). Interdiffusion leads to a broadened but still uniform QW, with group V and group III elements having separate QW width changes,  $\Delta_{wV}$  and  $\Delta_{wIII}$ . A diffusion ratio is defined similarly by  $\kappa \equiv \Delta_{wV}/\Delta_{wIII}$ . The morphological profile shown in Fig. 6(f) clearly indicates that  $\kappa > 1$  [5].

Finite element computations are used to quantitatively evaluate the strain across the QW which leads to the surface undulation observed by STM. The computation is carried out similar to that of Ref. [5]. However, in the earlier computation a model solid with isotropic elastic properties was assumed. Here we use the more accurate anisotropic elastic properties with cubic symmetry.

First, let us consider the Fickian model to describe the interdiffusion profile. In the STM image (Fig. 6(f)), we measured a surface undulation amplitude “A” of 0.4 Å. From this value, we can determine by finite element computation a set of allowable values for  $\Delta_V$  and  $\Delta_{III}$ , as shown by dashed line in Fig. 7. From PL measurement we found a 110 meV blue shift for this sample. Values of  $\Delta_V$  and  $\Delta_{III}$  which yield this PL shift are shown as the solid line in Fig. 7. Combining these two results, we deduce values of  $\Delta_V \approx 1.3$  nm and  $\kappa \approx 2.6$ . This  $\kappa$  value is somewhat larger than the value of  $\kappa \approx 1.7$  obtained previously where isotropic elastic properties were used [5]. Repeating the finite element analysis (as in Fig. 8) for the square well model yields a value of  $\kappa \approx 2.4$ . Such values are consistent with studies of similarly intermixed quantum wells using absorption to measure the heavy hole-light hole splitting [11]. The nearly vertical PL and STM curves in Fig. 7 for  $\kappa > 1.5$  shows how the results become insensitive to Group III intermixing lengths below one or two monolayers.

In our previous analysis [5] we assumed the applicability of the Fickian model for describing the quantum well intermixing. However, subsequent analysis of x-ray diffraction results indicated that a square well model might provide a better description [12]. Thus, we compare in Fig. 8 our experimental results with profiles predicted by these two models. We see that the square well model does indeed fit the data better — the long compressive tail seen in the Fickian profile far from the well is absent for both the experimental and the square well profiles, and the separation between the top maxima at the two interfaces is also better described by the square well model. It should be noted, however, that distinguishing these differences between square well and Fickian model results is probably near the current limit of accuracy of the STM results [6]. Complementary simulations of double crystal x-ray curves for these samples confirm the necessity of sharp interfaces and the overall suitability of the square well model for describing the results [12].

### 3.3 Mechanism of Intermixing

Two interpretations can explain the different strain development with varying implantation range. In both interpretations we assume that group V defects (interstitial or vacancy) only cause diffusion on the group V sublattice, and group III defects only cause diffusion on the group III sublattice. In the deep implantation case, both group V and group III defects are simultaneously produced at the MQW region, so it is possible that group V and group III elements will intermix roughly equally. However, in the shallow implantation case, defects are produced in the cap layer far away from the MQW region, and during the subsequent annealing the defects need to diffuse a long distance to reach the MQW region and cause intermixing. For our first interpretation, we assume that group V defects (P interstitial or vacancy) diffuse much faster than group III defects (In interstitial or vacancy), so there will be more group V defects reaching the MQW during the anneal time to cause group V preferred intermixing. As an alternative interpretation, one could assume that the “+1” model established in Si [13,14] will also apply in InP: most vacancies and interstitials produced by implantation will recombine at the initial stage of annealing, leaving behind (roughly) only those additional interstitials introduced by implantation. Since we use P ions in the implantation, presumably P interstitials are left after initial annealing, and they will diffuse to the MQW region to cause group V intermixing.

However, if this interpretation based on the “+1” model is correct, then if In ions instead of P ions are used for implantation, a preferred group III intermixing should be observed, leading to a compressively strained well and tensilely strained interface. We therefore undertook an experiment using In implantation to test this interpretation. Figure 9 shows an STM image of a sample prepared by shallow In implantation followed by thermal annealing. Contrary to the prediction of “+1” model, we still clearly observe a tensilely strained (*i.e.* dark) well, and compressively strained interfaces. Note however that a significant asymmetry is seen between the left and right interfaces in Fig. 9; a similar asymmetry has been occasionally observed in STM images of the other samples (both as-grown and implanted), although the magnitude of the asymmetry appears to vary with imaging conditions (*i.e.* sample-tip voltage, and tip characteristics). We attribute this asymmetry to features of the original growth of the InGaAs quantum wells, as further discussed in the following section. In any case, the result of Fig. 9, with the tensilely strained well, clearly rules out the interpretation based on the “+1” model. Rather, it favors the first interpretation that P related defects diffuse faster than In related defects. This conclusion is strongly supported by recent work on QWs intermixed by incorporating low growth-temperature InP layers near the QWs [11,15]. Absorption and x-ray measurements on such structures after annealing produce preferential group V interdiffusion and suggest a P interstitial defect mechanism is at work in both these intermixing techniques.

Comparing Figs. 6(b) and (d) carefully, it can be seen that the undulation in Fig. 6(d) is slightly larger than that in Fig. 6(b). While the line scan average of Fig. 6(d) is  $0.40 \pm 0.05$  Å as shown in Fig. 6(f), a similar line scan average for Fig. 6(b) is only  $0.30 \pm 0.05$  Å. This means that the group V to group III interdiffusion ratio is larger for Fig. 6(d), which corresponds to the bottom well of the 20 period MQW stack. This can be nicely explained by the first interpretation above that group V related defects are fast diffusers—since the defects need to diffuse over longer distances to reach the bottom well, less group III defects will arrive there and the  $\Delta_V/\Delta_{III}$  ratio is correspondingly increased. However, we also note that the proximity of the top of the stack to the implantation region also means that a small number of implanted ions will tail into the top well,

thereby also possibly contributing to the observed reduction in the  $\Delta V/\Delta III$  ratio.

Finally, we note that since the Si doping level in wafer B is substantially lower than that in wafer A ( $2 \times 10^{17} \text{ cm}^{-3}$  compared to  $8 \times 10^{18} \text{ cm}^{-3}$ ), it is necessary to consider a possible doping level dependence of the QW intermixing process. To this end, we implanted *through* the MQW region of wafer B with 4.7 MeV P ions and annealed at 740° C for 90 s. STM and XRD measurements [12] on those samples revealed very little strain development in the QWs, similar to the results from wafer A. We thus conclude that the different strain development discussed above for deep-implanted samples from wafer A and shallow-implanted samples from wafer B is indeed due to the difference in the implantation range.

### 3.4 As-grown Quantum Wells

In addition to providing information on the intermixed QWs, the STM results reported here can be used to examine characteristics of the as-grown QWs themselves. Several processes involving atom surface segregation and exchange are known to occur during InGaAs/InP heterostructure growth [16,17], resulting in an asymmetry relative to the growth direction of the heterostructures. Although as shown below the expected magnitude of such effects in the STM images is quite small ( $\approx 0.1 \text{ \AA}$ , which is the same as our estimated uncertainty for interpreting the STM images purely in terms of strain-induced topographic effects [5,6]), results from other techniques such as XRD also have considerable uncertainty in observing these effects. Thus, we consider here a combination of XRD and STM results in determining possible growth induced asymmetries in the as-grown InGaAs/InP heterostructures.

Double crystal XRD readily (and very precisely) provides two pieces of information on the average MQW structure, the mean strain and the period. This information comes from the position of the MQW 0th order peak relative to the substrate peak, and their spacing respectively. To extract more information on the actual width and shape of the QWs the envelope of the satellite peaks also has to be fitted. To be able to do this it is important to understand the growth processes that occur when switching from the growth of InP to InGaAs and back again. The dominant process that is believed to occur concerns an exchange of the group V species. When growing the first monolayer of InGaAs on InP an As/P exchange occurs at the InP surface [16], resulting in the formation of a thin InAsP layer between the InP and InGaAs layers. This InAsP is compressively strained relative to InP. A similar process occurs on the InGaAs surface resulting in the formation of a tensilely strained InGaAsP layer between the InGaAs and InP layers. There is also a tendency to carry over As from the InGaAs growth into the following InP barrier [17], resulting in slightly compressively strained InAsP barrier material. This As carry over can be seen in STM images (Figs. 4(a), 6(a) and (c)) as the bright spots in the barrier layers. Adding these layers into an x-ray simulation package, and optimizing, results in the fit shown in Fig. 10(a). The parameters for this fit are given in Table I. To obtain a good fit it was found to be necessary to have one interface of the QW compressively strained and the other tensilely strained. Note, however, that the interface layers used to accomplish this are only one or two monolayers in thickness. The mean strain and width of the QW are tightly constrained for a good fit. The general features observed in this fit are true for all of the InGaAs/InP MQW structures grown in this growth system, and are not just peculiar to this one sample.

Various features in the x-ray envelope can be associated with physical features of the sam-

ple. The separation of the minima at approximately  $\pm 4000$  arcsec defines the QW/barrier thickness ratio, the absolute position of those minima are dominated by the QW strain. The depth of the modulation in the envelope is controlled by the degree of strain at the interfaces. The range of values that would provide a good fit were severely limited when having to satisfy all of these features simultaneously. There are two features that are not fitted well by the simulation, these are the weak shoulders observed on the main satellite peaks, and the low intensity of the  $\pm 1$  order peaks. The shoulders seem to indicate that there is a region of the superlattice with a different periodicity. This is unlikely since after intermixing they are no longer present, and intermixing is not expected to change the fundamental periodicity of the structure. The low intensity of the  $\pm 1$  order peaks is sometimes observed in other similar samples and can be removed by slightly modifying the growth conditions. When this is done all the other peaks remain the same and the envelope then fits the x-ray simulation for all peaks. Since the  $\pm 1$  peaks are associated with low spatial frequencies the intensity reduction might be associated with random variations from period to period within the superlattice caused by interface roughness. This might also cause the apparent variations in periodicity observed (the weak shoulders).

The composition profile from the x-ray fit can be used with the elastic model to generate a surface topography map of the cleaved surface observed by STM, and compared to the actual STM images. Based on the model of Table I, the resulting surface profile is shown in Fig. 11(a). This profile should be compared to those of Figs. 4(c) and 6(e). The most obvious common feature of these three profiles is the peak on the right edge of the QW associated with a thin compressively strained layer. However, a tensile layer on the left edge is only hinted at in Fig. 6(e), and Fig. 4(c) also contains a minimum at the center of the QW not predicted by the x-ray model. Examination of many other STM profiles of the as-grown QWs reveals that the minimum seen near the center of the QW in Fig. 4(c) arises simply from a fluctuation in the alloy content of that portion of the QW. Profiles for which such fluctuation effects are not so apparent (obtained by vertically averaging over a larger region of QW than that of Fig. 4(a)) are shown in Fig. 12. For reference, the interface between QW and barrier regions are marked by dashed lines in both Figs. 11 and 12, with the QW defined in this case by the region containing  $\text{In}_{0.53}\text{Ga}_{0.47}$  anions (as specified in Table I for Fig. 11(a), or as readily seen in the STM images for Fig. 12). The profiles of Fig. 12 are seen to have a topographic maximum on the right side of the well and a minimum on the left, in agreement with the XRD derived result of Fig. 11(a).

In addition to confirming the general features of the x-ray model, STM indicates an interesting feature that x-ray analysis does not unambiguously identify. Examination of the STM profiles indicates an additional reduction in surface height in the barrier region near the InGaAs on InP interface. As discussed in the previous section, this asymmetry has been seen to varying degrees in many of our as-grown or implanted samples; the effect is clearly seen in Figs. 4(a), 4(c), 5, and 12(a), and Fig. 9 show a somewhat extreme example of this asymmetry. Although electronic effects in the STM imaging could contribute to the magnitude of this effect, we nonetheless seek a strain induced topographic origin for the feature as a possible candidate for its origin. This feature, a reduction in surface height prior to the InGaAs on InP interface, is clearly not present in the model profile of Fig. 11(a), and the only way to introduce such an effect is to add a tensile layer at this interface. For this to occur the understanding of the growth process at that interface has to be modified. The only way to introduce tensile strain into an InP layer is by adding Ga to form InGaP or InGaAsP. This could happen if Ga/In exchange occurs when the first monolayer of InGaAs is

deposited on the InP barrier material. A compressive layer is still required on top of this tensile layer, which could occur due to In segregation effects during the growth of the InGaAs QW [Mésrine]. This would result in the formation of an In rich InGaAs alloy close to the InGaAs on InP interface as indicated in Table II. The x-ray simulation for this type of structure is given in Fig. 10(b) and gives a similar degree of fit to that in Fig. 10(a). In the x-ray measurement, the effect of a tensile layer right next to a compressive layer of equal magnitude does not contribute to the overall strain in the QW and as such has no effect on the position of the 0th order MQW peak. The resulting surface topographical map is shown in Fig. 11(b); it results in a slightly better fit to the STM data, although the magnitude of the topographic minimum near the right hand interface is not as large as that seen in the experiment.

Concerning the possibility of Ga/In exchange at the InGaAs on InP interface, it is important to note that in the switching sequence used to grow these samples, In and Ga were introduced into the growth chamber one second before the As when switching from InP to InGaAs growth. This somewhat unconventional scheme was used to reduce the effect of As/P exchange [19]. It is possible that this switching sequence has resulted in the formation of a thin tensile InGaP/InGaAsP layer, and that In segregation occurs under these growth conditions. Further study of this process, using QWs grown with the more conventional switching scheme, is required to more confidently determine the origin of this growth asymmetry seen in the STM images.

#### 4 CONCLUSION

Cross-sectional STM is used to study the QW interface change and strain development during intermixing. Intermixing is clearly observed, with the QW alloy layer becoming wider after implantation and annealing. No significant strain change is observed for a sample with ions implanted through the MQW, but a shallow implantation is found to lead to a tensile strained well and compressively strained interface. A group V to group III interdiffusion length ratio is determined by a combination of finite element computation of strain relaxation and computation of PL transition energy change. It is found that a simple square well model gives a somewhat better fit to the strain profile than a Fickian model. The different group V and group III interdiffusion lengths in the shallow implantation case is interpreted in terms of a larger supply of group V defects to the MQW region caused by a faster diffusion of P related defects compared with In related defects. Study of the STM images of as-grown QWs coupled with x-ray measurements reveals interesting features related to the gas switching sequence used in the QW growth.

#### 5 ACKNOWLEDGMENTS

This work was supported by grants from the U.S. National Science Foundation (DMR-9985898) and the National Science and Engineering Research Council of Canada.

- [1] See for example, D. G. Deppe and N. Holonyak Jr., *J. Appl. Phys.* **64**, R93 (1988).
- [2] S. Charbonneau, P. J. Poole, P. G. Piva, G. C. Aers, E. S. Koteles, M. Fallahi, J.-J. He, J. P. McCaffrey, M. Buchanan, M. Dion, R. D. Goldberg, and I.V. Mitchell, *J. Appl. Phys.* **78**, 3697 (1995).
- [3] For a review, see R. M. Feenstra, *Semicond. Sci. Technol.* **9**, 2157 (1994).
- [4] H. Chen, R. M. Feenstra, R. S. Goldman, C. Silfvenius, and G. Landgren, *Appl. Phys. Lett.*

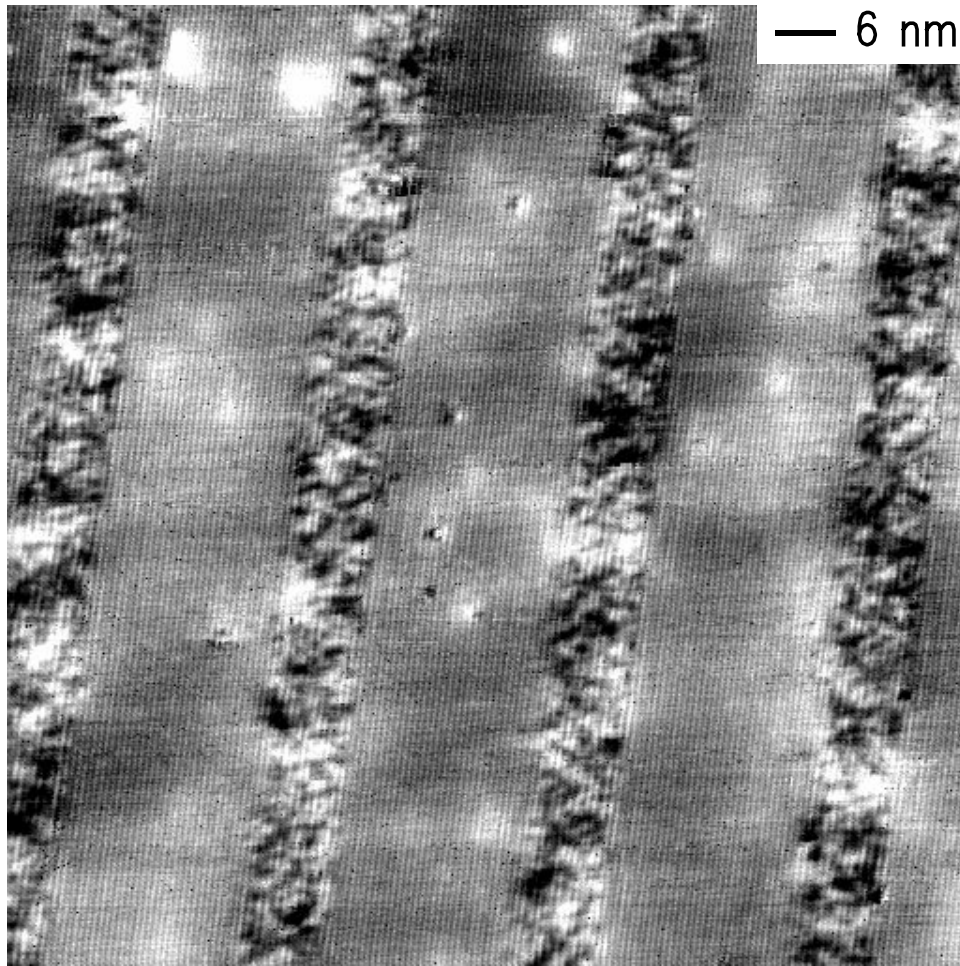
- 72**, 1727 (1998).
- [5] H. Chen, R. M. Feenstra, P. G. Piva, R. D. Goldberg, I. V. Mitchell, G. C. Aers, P. J. Poole, and S. Charbonneau, *Appl. Phys. Lett.* **75**, 79 (1999).
  - [6] R. M. Feenstra, *Physica B* **273-274**, 796 (1999).
  - [7] P. G. Piva, R. D. Goldberg, I. V. Mitchell, H. Chen, R. M. Feenstra, G. C. Weatherly, D. W. McComb, G. C. Aers, P. J. Poole and S. Charbonneau, *Appl. Phys. Lett.* **72**, 1599 (1998).
  - [8] J. Cibert and P. M. Petroff, *Phys. Rev. B* **36**, 3243 (1987).
  - [9] J. Micallef, E. H. Li, and B. L. Weiss, *J. Appl. Phys.* **73**, 7524 (1993).
  - [10] J. Z. Wan, J. G. Simmons, and D. A. Thompson, *J. Appl. Phys.* **81**, 765 (1997).
  - [11] J. E. Haysom, G. C. Aers, S. Raymond, and P. J. Poole, *J. Appl. Phys.* **88**, 3090 (2000).
  - [12] P. G. Piva *et al.*, unpublished
  - [13] M. D. Giles, *J. Electrochem. Soc.* **138**, 1160 (1991).
  - [14] D. J. Eaglesham, P. A. Stolk, H.-J. Gossmann, and J. M. Poate, *Appl. Phys. Lett.* **65**, 2305 (1994); L. Pelaz, G. H. Gilmer, m. Jaraiz, S. B. Herner, H.-J. Gossmann, D. J. Eaglesham, G. Hobler, C. S. Rafferty, and J. Barbolla, *Appl. Phys. Lett.* **73**, 1421 (1998).
  - [15] J.E. Haysom, G.C. Aers, S. Raymond, and P.J. Poole, *Solid State Comm.* (in press).
  - [16] R.T. Rongen, A.J.C. van Rijswijk, M.R. Leys, C.M. van Es, H. Vonk, and J.H. Wolter, *Semicond. Sci. Technol.* **12**, 974 (1997); G-J. Shiau, C-P. Chao, P.E. Burrows, and S.R. Forrest, *J. Appl. Phys.* **77**, 201 (1995); R. Benzaquen, A.P. Roth, and R. Leonelli, *J. Appl. Phys.* **79**, 2640 (1996).
  - [17] A. Antolini, P.J. Bradley, C. Cacciatore, D. Campi, L. Gastaldi, F. Genova, M. Iori, C. Lamberti, C. Papuzza, and C. Rigo, *J. Elect. Mater.* **21**, 233 (1992); X.S. Jiang, A.R. Clawson, and P.K.L. Yu, *J. Cryst. Growth*, **147**, 8 (1995); J. Wagner, M. Peter, K. Winkler, and K.-H. Bachem, *J. Appl. Phys.* **83**, 4299 (1998).
  - [18] M. Mesrine, J. Massies, C. Deparis, N. Grandjean, and E. Vanelle, *Appl. Phys. Lett.* **68**, 3579 (1996); M. Mesrine, J. Massies, C. Deparis, N. Grandjean, E. Vanelle, and M. Leroux, *J. Cryst. Growth*, **175**, 1242 (1997).
  - [19] G-J. Shiau, C-P. Chao, P.E. Burrows, and S.R. Forrest, *J. Appl. Phys.* **77**, 201 (1995); A.P. Roth, P. Levesque, R.W.G. Syme, D.J. Lockwood, G.C. Aers, T.S. Rao, and C. Lacelle, *J. Appl. Phys.* **80**, 4033 (1996).

Table 1 Compositional profile ( $\times 20$ ) derived from x-ray analysis of sample B: Conventional As/P exchange model. Growth order is from layer 1 to 6.

<i>Layer</i>	<i>Thickness(nm)</i>	<i>Material</i>	<i>x</i>	<i>y</i>
1	0.5	InAs(y)P(1-y)	-	0.380
2	4.9	In(1-x)Ga(x)As	0.470	-
3	0.5	In(1-x)Ga(x)As(y)P(1-y)	0.470	0.565
4	0.3	InAs(y)P(1-y)	-	0.350
5	0.3	InAs(y)P(1-y)	-	0.150
6	18.7	InAs(y)P(1-y)	-	0.015

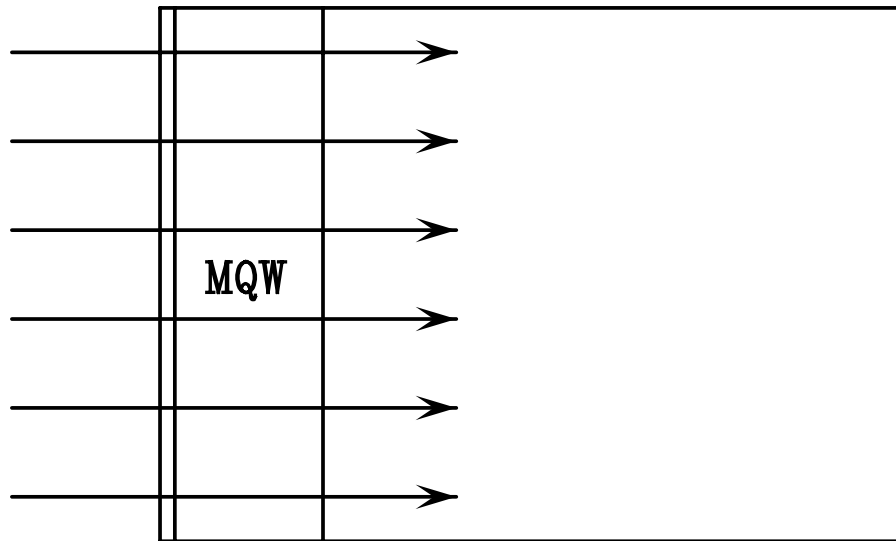
Table 2 Compositional profile ( $\times 20$ ) derived from x-ray analysis of sample B: Ga/In exchange model. Growth order is from layer 1 to 7.

<i>Layer</i>	<i>Thickness(nm)</i>	<i>Material</i>	<i>x</i>	<i>y</i>
1	0.3	In(1-x)Ga(x)P	0.320	-
2	0.5	In(1-x)Ga(x)As	0.080	-
3	5.2	In(1-x)Ga(x)As	0.470	-
4	0.5	In(1-x)Ga(x)As(y)P(1-y)	0.470	0.668
5	0.3	InAs(y)P(1-y)	-	0.180
6	0.3	InAs(y)P(1-y)	-	0.100
7	18.1	InAs(y)P(1-y)	-	0.015

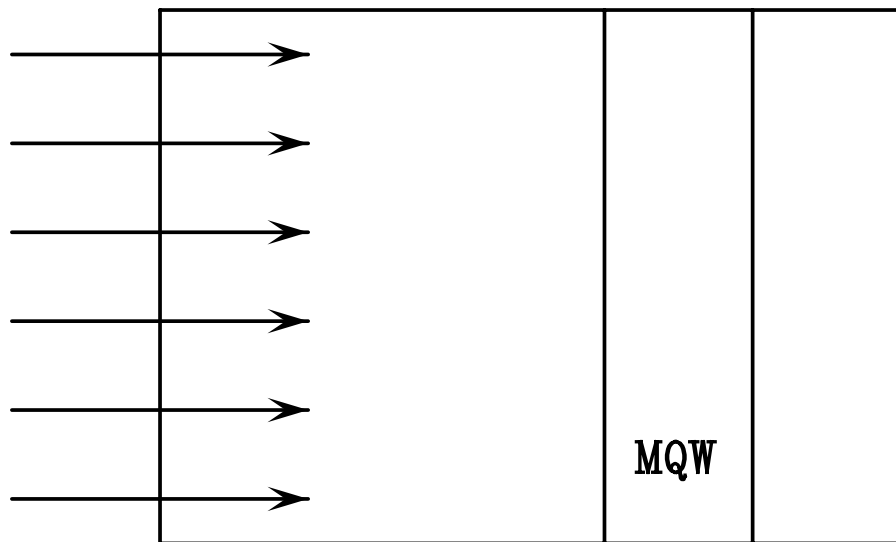


←  
Growth Direction

Figure 1 Cross-sectional STM image of InGaAs/InP MQW stack. Image was acquired at a sample voltage of +2.5 V. The grey scale range is 0.06 nm. Layer growth direction is from right to left.



(a)



(b)

Figure 2 Illustration of ion implantation range for the two types of samples studied. Wafer A has a thin (19 nm) cap layer with 534 nm wide MQW stack, and 1 MeV P ions are implanted through the MQW stack to a depth of 0.94  $\mu\text{m}$ ; wafer B has a thick (1.56  $\mu\text{m}$ ) cap layer with 504 nm wide MQW stack, and 0.5 MeV P ions are implanted into the cap layer to a depth of 0.52  $\mu\text{m}$  without reaching the MQW stack.

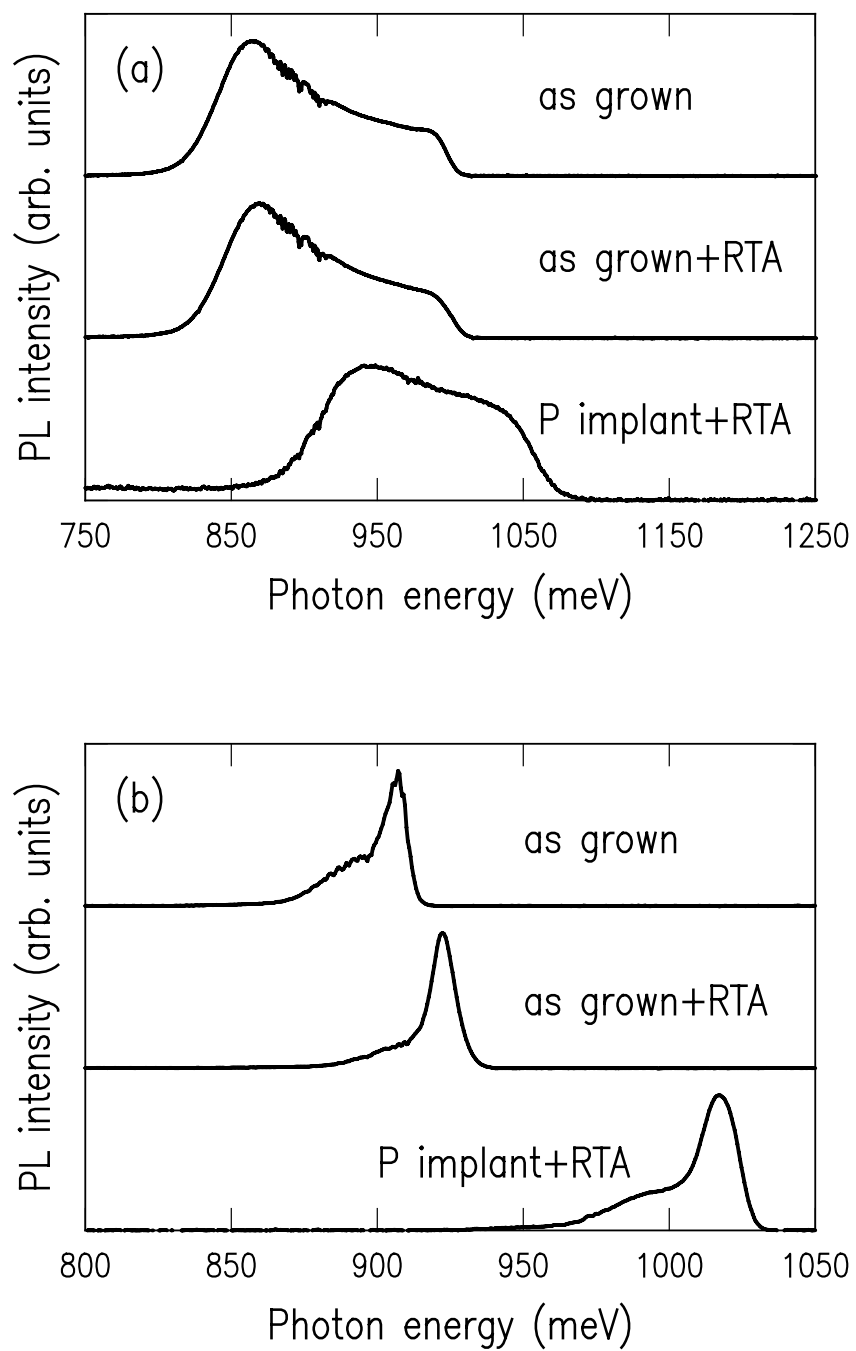


Figure 3 Low temperature (4.2K) PL spectra for InGaAs/InP MQW samples: (a) wafer A; (b) wafer B.

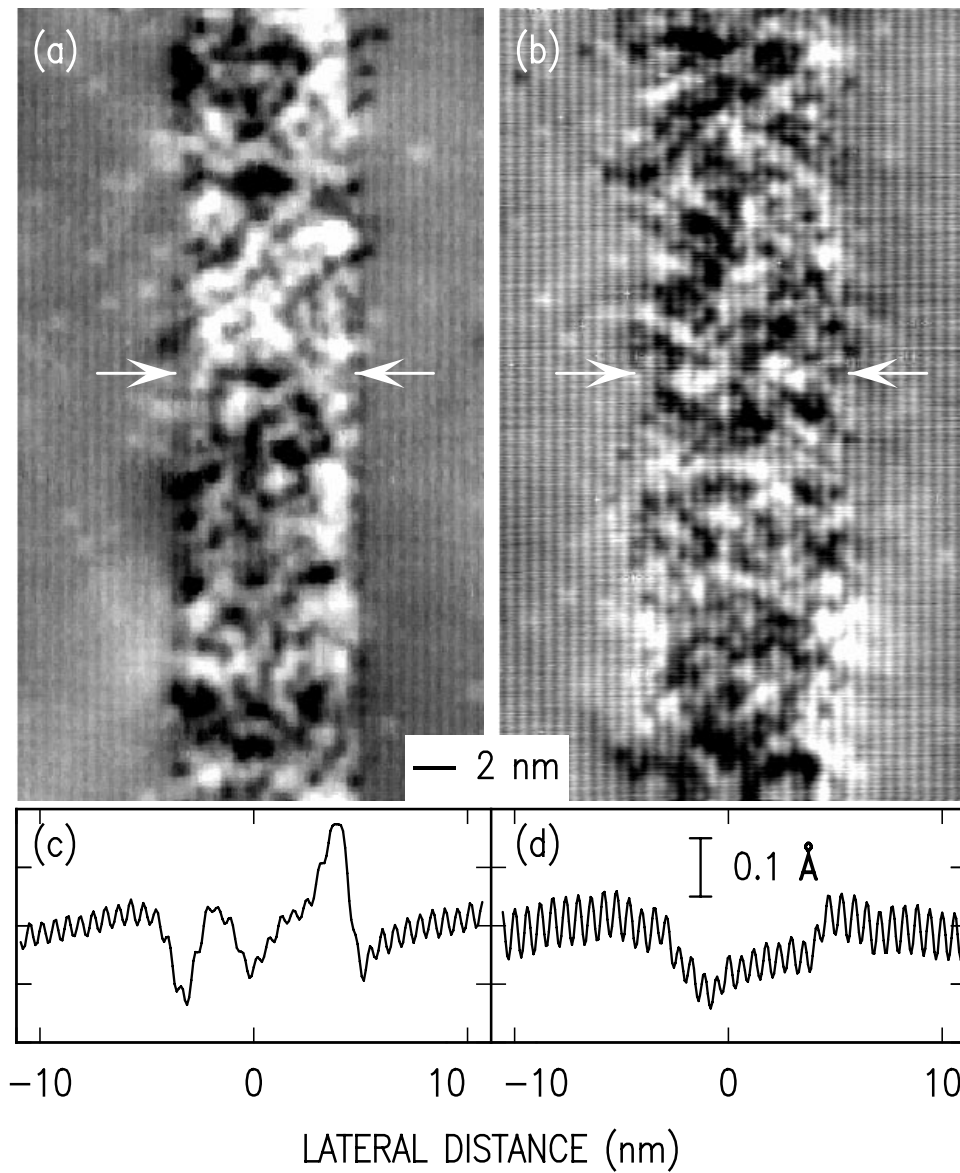


Figure 4 Cross-sectional STM images of InGaAs/InP heterostructures from wafer A: (a) unimplanted (as-grown + RTA); (b) implanted + RTA. Images were acquired at sample bias voltages of +1.8 V and +2.0 V, respectively. Grey scale ranges are 0.06 nm and 0.05 nm, respectively. An average of the topographic line scans is shown in (c) and (d). The growth direction is from right to left across the images.

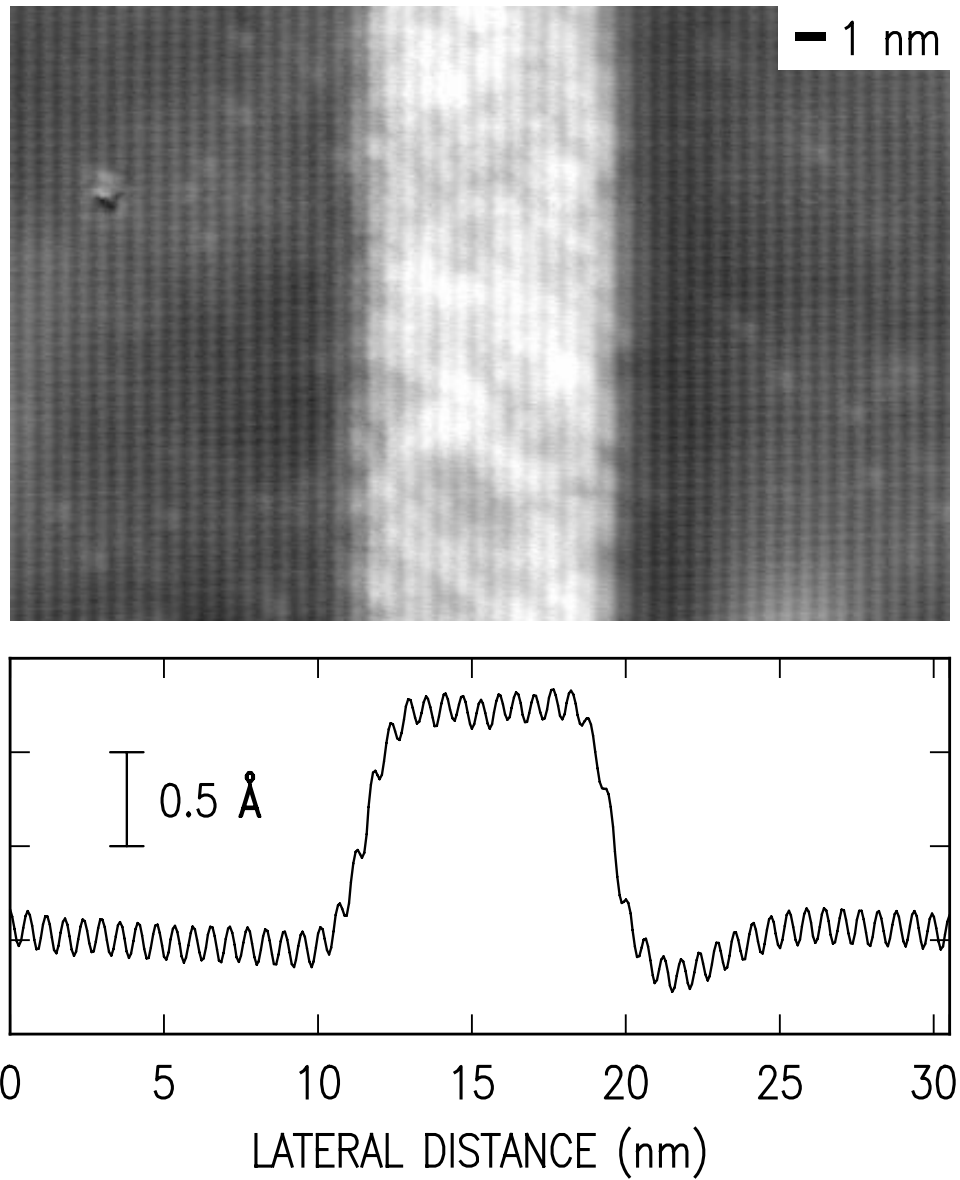


Figure 5 Cross-sectional STM images of InGaAs/InP heterostructures from an unimplanted (as-grown + RTA) sample of wafer A. Image was acquired at sample bias voltage of -1.8 V. Grey scale range is 0.25 nm. An average of the topographic line scans is shown below the image.

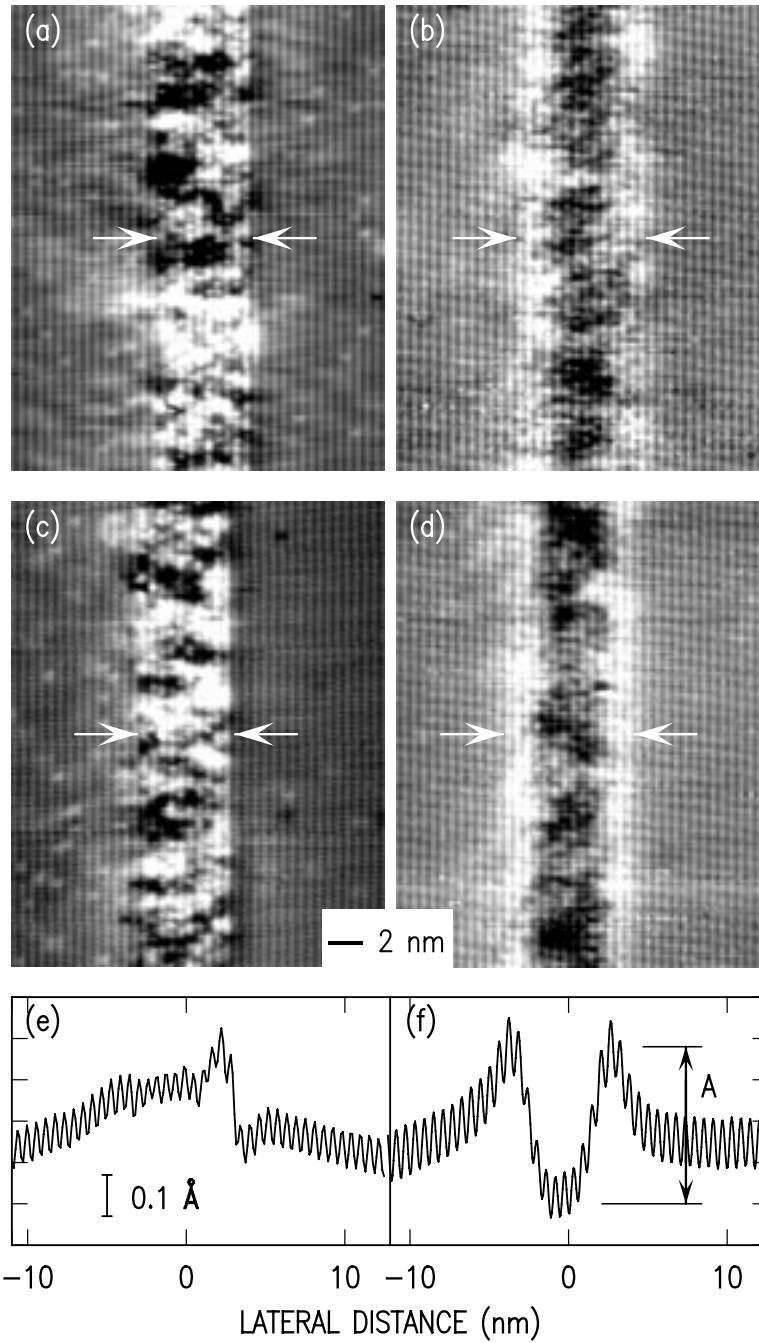


Figure 6 Cross-sectional STM images of InGaAs/InP heterostructures from wafer B: (a) top layer of as-grown sample; (b) top layer of implant + RTA sample; (c) bottom layer of as-grown sample; (d) bottom layer of implant + RTA sample. An average of the topographic line scans is shown in (e) and (f), with the undulation amplitude  $A$  indicated in (f). Images were acquired at sample bias voltages of +2.5 and +2.0 V for as-grown and implant+RTA samples, respectively. Grey scales are 0.05, 0.05, 0.05, and 0.06 nm for image (a)–(d), respectively. The growth direction of the layers is from right to left. Arrows indicate approximate width of the quantum wells.

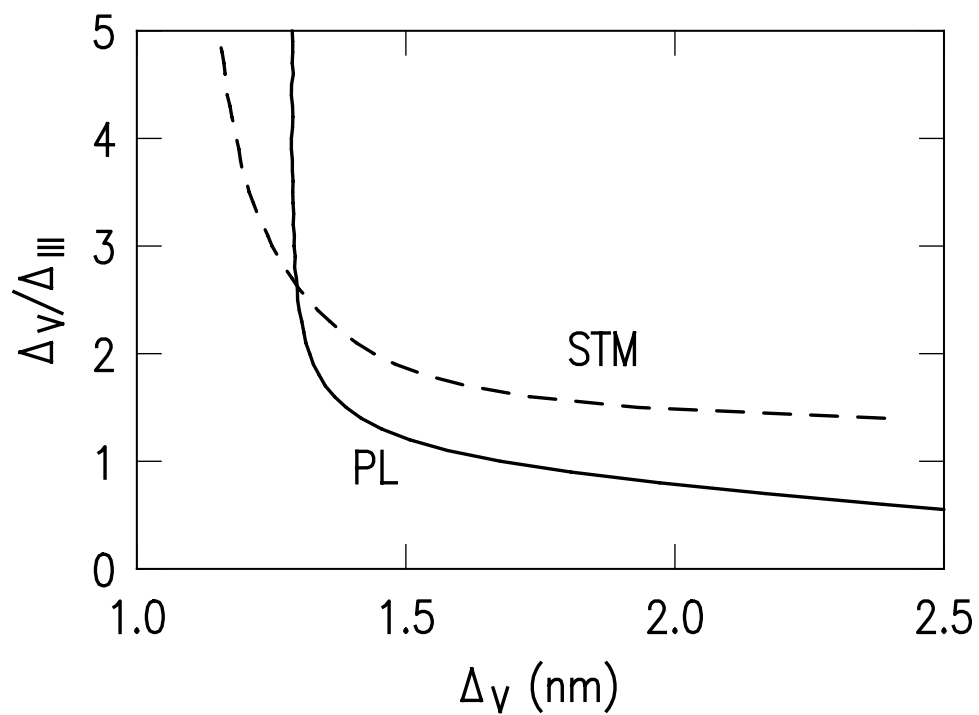


Figure 7 Determination of group V to group III interdiffusion length ratio. Dashed line shows the combination of  $\Delta_V$  and  $\Delta_V/\Delta_{III}$  that gives an undulation amplitude of  $0.4 \text{ \AA}$ , solid line shows the possible values of  $\Delta_V$  and  $\Delta_V/\Delta_{III}$  that gives a PL blue shift of 110 meV.

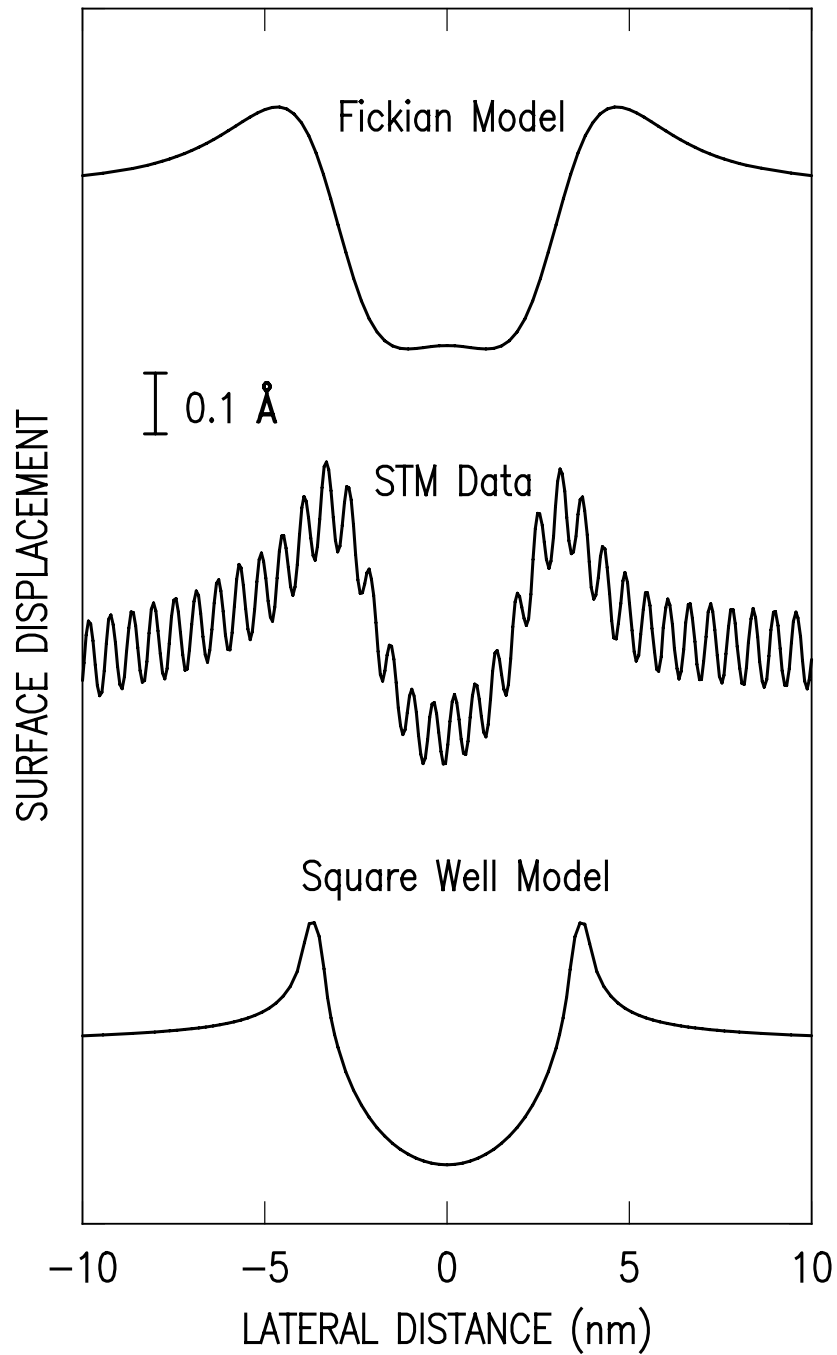


Figure 8 Comparison of surface undulation profile. The middle line shows the STM line scan, the top and bottom lines show those undulation profiles predicted by using Fickian model and square well model, respectively (using values of  $\Delta v$  and  $\kappa$  determined earlier by a combination of STM and PL).

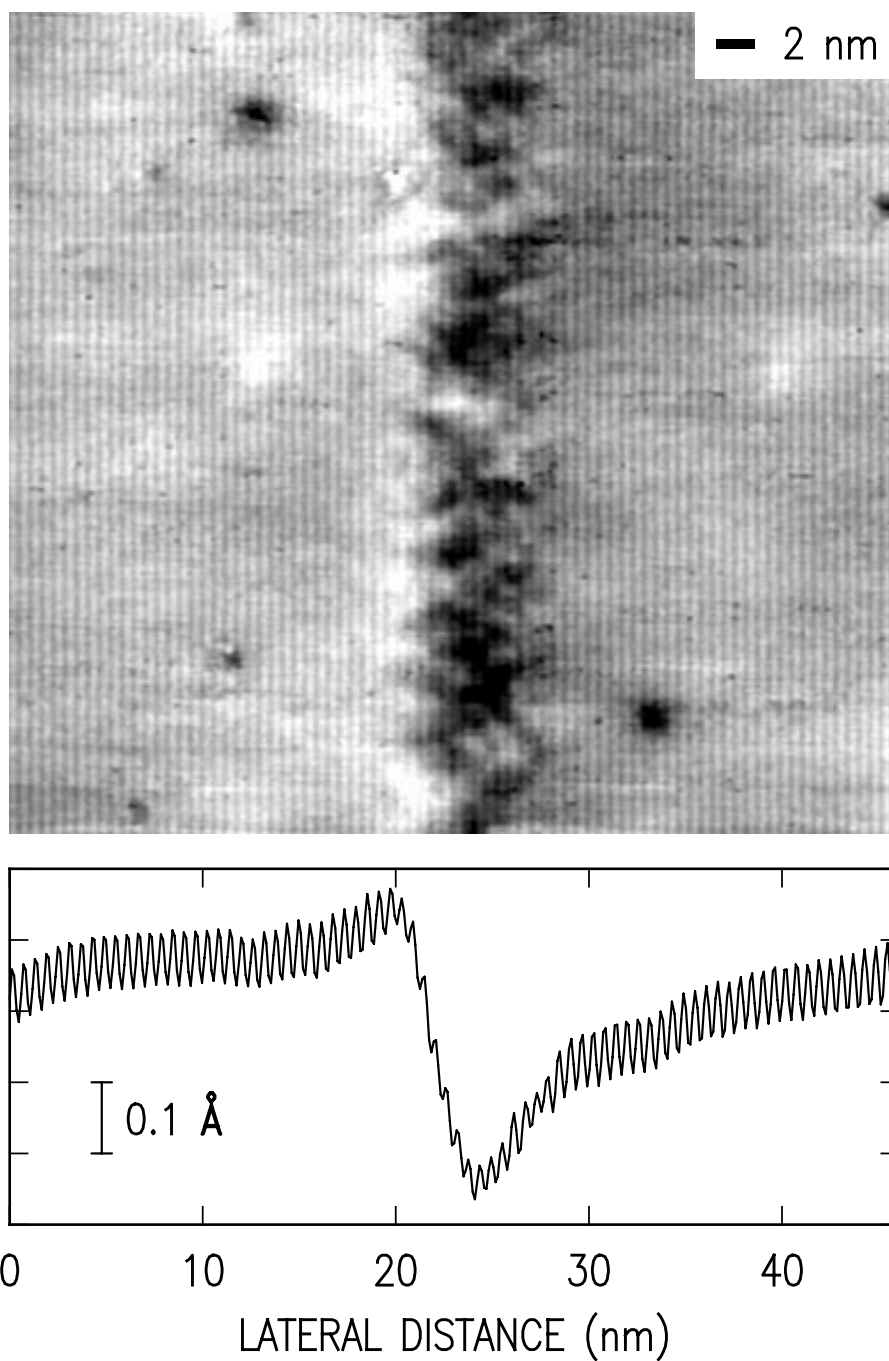


Figure 9 Cross-sectional STM image of InGaAs/InP heterostructure, intermixed using In implantation followed by thermal annealing. Image was acquired at sample bias voltage of +2.5 V. Grey scale range is 0.06 nm. An average of the topographic line scans is shown below the image.

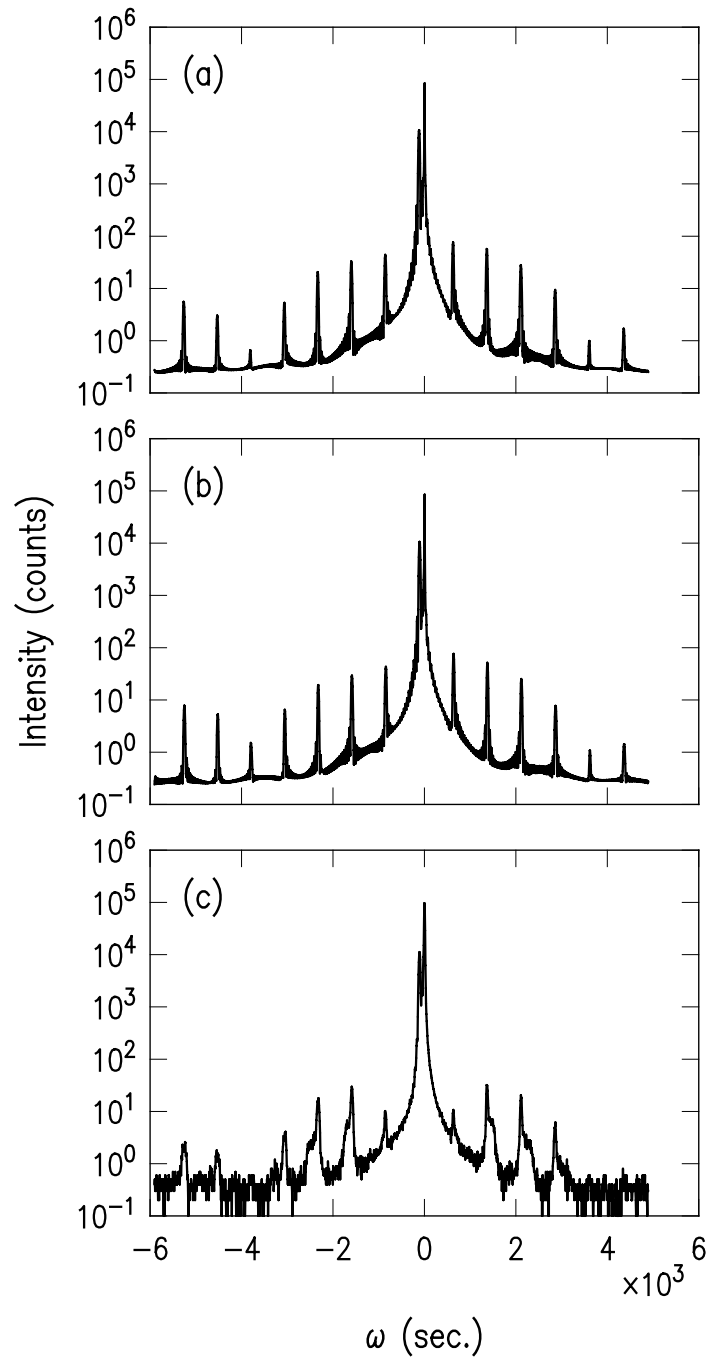


Figure 10 Theoretical and experimental double crystal x-ray curves for as-grown wafer B: (a) theoretical curve fitted using the conventional As/P exchange model of Table 1, (b) theoretical curve fitted using the Ga/In exchange model of Table 2, appropriate to the growth sequence used, and (c) experimental curve.

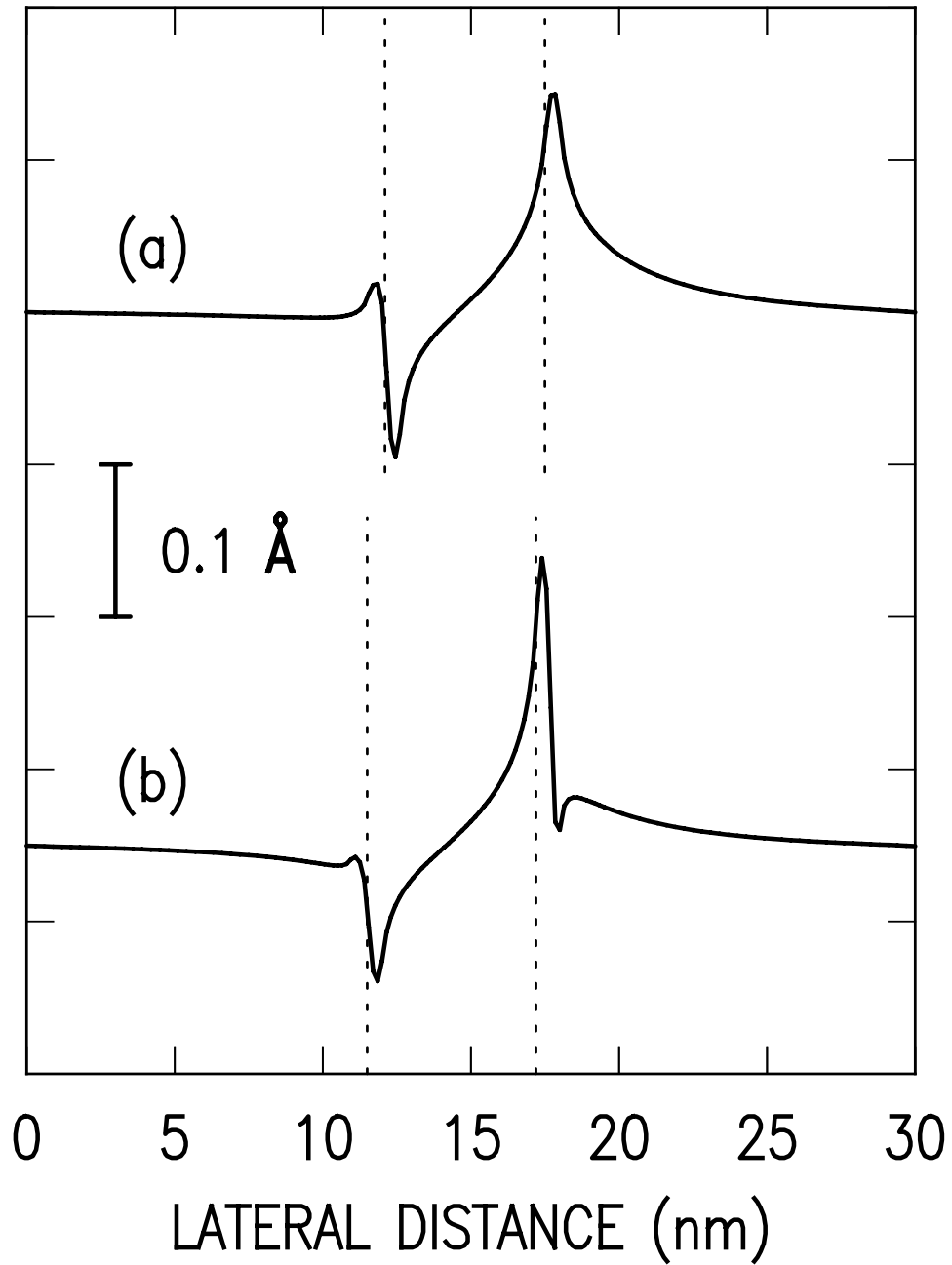


Figure 11 Surface undulation profile for as-grown wafer B calculated using (a) the conventional As/P exchange model of Table 1 and (b) the Ga/In exchange model of Table 2, appropriate to the growth sequence used. The dashed lines indicate the boundary between QW and barrier regions, as discussed in the text.

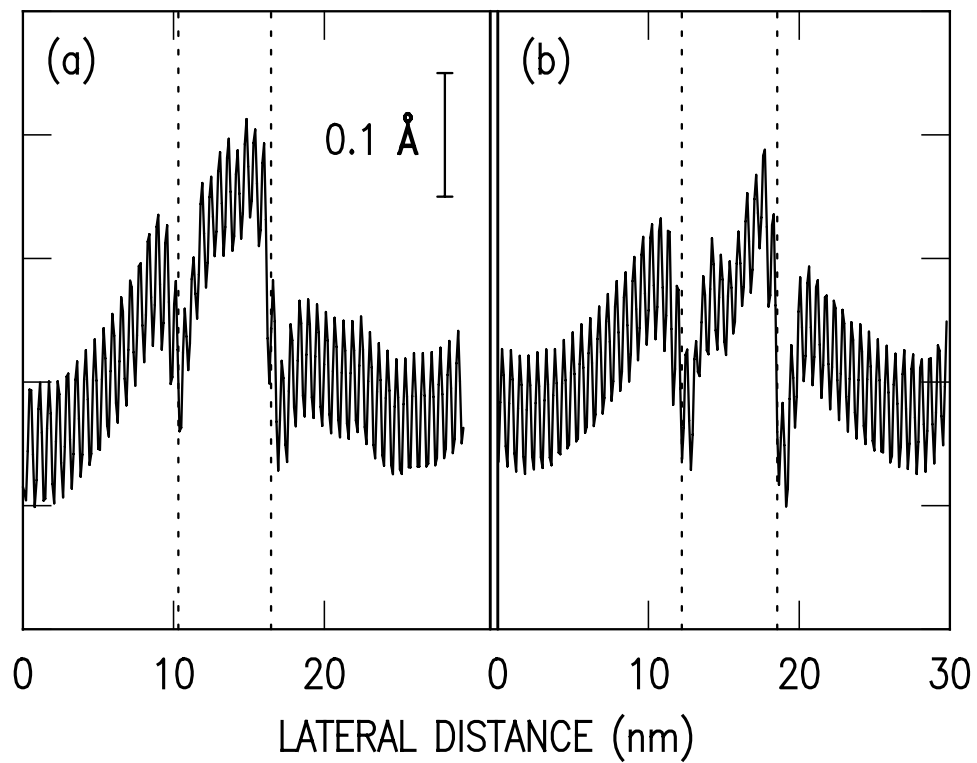


Figure 12 Typical experimental STM surface undulation profiles for as-grown wafer B. The growth direction of the layers is from right to left. The dashed lines indicate the boundary between QW and barrier regions, as discussed in the text.